

# Reductive cation for scalable wide-bandgap perovskite solar cells in ambient air

Guang Yang<sup>1,2</sup>, Hangyu Gu<sup>1</sup>, Jun Yin<sup>3</sup>, Chengbin Fei<sup>1</sup>, Zhifang Shi<sup>1</sup>, Xiaoqiang Shi<sup>1</sup>, Xingjian Ying<sup>1</sup>, Jinsong Huang<sup>1,4\*</sup>

<sup>1</sup>Department of Applied Physical Sciences, The University of North Carolina at Chapel Hill, NC 27599, USA

<sup>2</sup>Department of Electrical and Electronic Engineering, Photonic Research Institute (PRI), Research Institute of Smart Energy (RISE), Research Institute for Advanced Manufacturing (RIAM), The Hong Kong Polytechnic University, Hung Hom, Kowloon, Hong Kong, China

<sup>3</sup>Department of Applied Physics, The Hong Kong Polytechnic University, Hung Hom, Kowloon, Hong Kong, China

<sup>4</sup>Department of Chemistry, The University of North Carolina at Chapel Hill Chapel Hill, NC 27599, USA

**Abstract:** High-performance wide-bandgap (WBG) perovskite solar cells (PSCs) are expected to play key role in next-generation multi-junction solar cells. However, there are still several challenges to overcome, such as large photovoltage loss, poor stability, and scalable fabrication in ambient air, which hinders the commercialization of this technology. Here, we incorporate a reductive methylhydrazinium cation (MHy<sup>+</sup>) into WBG perovskites, which not only reduces defect density but also suppresses iodide oxidation and halide demixing, enabling scalable fabrication of efficient and stable WBG solar cells and modules in ambient air. Remarkably, the champion WBG PSCs achieve a power conversion efficiency (PCE) of 23.3% with an open-circuit voltage of 1.28 V, corresponding to a record low voltage loss of 0.37 V. The WBG minimodules deliver a stabilized PCE of 19.8% with an aperture area of 25 cm<sup>2</sup>. The minimodules can keep 94%

of the initial PCE after 700 hours of operation under continuous light soaking at 1 sun illumination at  $55 \pm 5$  °C. This work represents a viable route to the sustainable implementation of the solar energy.

## **Main**

Photovoltaics represent a significant advancement in the field of renewable energy, particularly in the pursuit of sustainable and environmentally friendly energy solutions. Metal halide perovskite solar cells (PSCs) have demonstrated significant advancements, achieving certified power conversion efficiency (PCE) exceeding 26%<sup>1,2</sup>. Despite the significant progress made in enhancing efficiency, the practical deployment of PSCs necessitates addressing critical issues concerning longevity and scalability<sup>3-6</sup>. Notably, research efforts have primarily concentrated on perovskite absorbers with bandgap within the range of 1.49-1.56 eV<sup>7-16</sup>. However, to surpass the theoretical efficiency limit of single-junction solar cells, the integration of wide-bandgap (WBG) perovskite (with a bandgap of 1.65-1.70 eV) with crystalline silicon in tandem solar cells has proven to be an exceptionally promising strategy to boost the efficiencies to a certified value of 33.9%<sup>17-20</sup>. Nevertheless, WBG PSCs have not achieved the same level of PCE compared to those with narrower bandgaps, with their efficiencies constrained by larger loss of open-circuit voltage ( $V_{OC}$ )<sup>21</sup>. Furthermore, scalability remains a crucial concern for WBG PSCs, especially since they are designed to be the top cells for wafer-sized silicon solar cells<sup>22,23</sup>.

Nearly all the reported high efficiency WBG perovskite and tandem cells were fabricated by spin-coating method. The reliance on glovebox-dependent solution-processes for upscaling is not commercially viable, making it imperative to produce WBG PSCs in ambient air for commercial production<sup>24</sup>. Unfortunately, there are only a few reports on scalable deposition of WBG perovskites in ambient condition, and none on efficient methylammonium (MA)-free WBG

PSCs<sup>21,25</sup>. The reaction of methylammonium ( $\text{MA}^+$ ) with formamidinium ( $\text{FA}^+$ ), which has been frequently observed, could change the stoichiometry of perovskites and thus limit the stability at elevated temperatures<sup>26,27</sup>. Moreover, mixed-halide WBG PSCs have particularly struggled with poor operational stability, primarily due to halide-demixing induced phase segregation<sup>28,29</sup>. Xu et al. demonstrated using triple-halide WBG perovskites (bandgap of 1.67 eV) to minimize phase segregation by decreasing the amount of  $\text{Br}^-$  to less than 20%<sup>30</sup>. In their study, chloride ( $\text{Cl}^-$ ) was incorporated to stabilize WBG perovskites by shrinking the lattice parameter and reducing Br content. Halide oxidation reaction has been proposed to explain halide segregation under operation conditions<sup>28</sup>. In this scenario, halide segregation is initiated by the oxidation of the most easily oxidized halide species, providing a gradient driving force for these species to migrate across the film. Therefore, minimizing or suppressing iodide oxidation may mitigate the halide-demixing induced phase segregation.

In this work, we report that the partial substitution of  $\text{Cs}^+$  or  $\text{FA}^+$  cation by a reductive methylhydrazinium ( $\text{MHy}^+$ ) cation in WBG perovskites ( $\text{Cs}_{0.25}\text{FA}_{0.75}\text{Pb}(\text{I}_{0.82}\text{Br}_{0.15}\text{Cl}_{0.03})_3$ ) with a bandgap of 1.65 eV can effectively inhibit the iodide oxidation and increase migration barrier for iodide ions, which mitigates phase segregation and improves the stability of WBG PSCs. Furthermore, hydrazinium group provides good defect passivation through Pb-N bonding, resulting in a record low  $V_{\text{OC}}$  deficit of 0.37 V for WBG PSCs and minimodules. Consequently, we obtain a champion efficiency of 23.3% for small-area WBG PSCs with a  $V_{\text{OC}}$  of 1.28 V. The uniformity of the films made by scalable blading process is also confirmed by the demonstration of efficient minimodules with a stabilized efficiency of 19.8%.

## Results

### Halide oxidation and ion migration in WBG perovskites

A reductive A-site cation, methylhydrazinium ( $\text{MHy}^+$ ), was incorporated to partially substitute either formamidinium ( $\text{FA}^+$ ) or  $\text{Cs}^+$  to form a triple-cation, triple-halide WBG perovskites, denoted as  $\text{MHy}_{1-x-y}\text{Cs}_x\text{FA}_y\text{Pb}(\text{I}_{0.82}\text{Br}_{0.15}\text{Cl}_{0.03})_3$ , where  $x$  (from 0.05 to 0.25) and  $y$  (from 0.55 to 0.75) are the percentages of Cs and FA, respectively.  $\text{MHy}^+$  has a larger ionic radius (264 pm) compared to the normally used A-site cations including  $\text{FA}^+$ ,  $\text{MA}^+$ , and  $\text{Cs}^+$ . Previous studies have reported that  $\text{MHy}^+$  can form both three-dimensional (3D) perovskites ( $\text{MHyPbBr}_3$ ) or two-dimensional (2D) perovskites ( $\text{MHy}_2\text{PbBr}_4$  or  $\text{MHy}_2\text{PbCl}_4$ ) depending on synthesis conditions<sup>31-35</sup>. However, it remains uncertain whether  $\text{MHy}^+$  can be partially incorporated into 3D WBG perovskites, despite the successful substitution of  $\text{MA}^+$  with  $\text{MHy}^+$  in  $\text{MAPbI}_3$ .<sup>36</sup> In addition, it is unclear whether  $\text{MHy}^+$  ions would exist in the formation of 2D perovskites in our WBG perovskite films or leave the films during thermal annealing. Therefore, we first investigated whether  $\text{MHy}^+$  can remain in the annealed WBG perovskite films using nuclear magnetic resonance (NMR) measurements. The  $^1\text{H}$  NMR spectra of the annealed WBG perovskite with  $\text{MHy}^+$ , or  $\text{MHy}$ -WBG perovskite, showed a signal peak belonging to  $\text{MHy}^+$  (2.6 ppm), which is identical to the peak from  $\text{MHyI}$  (**Supplementary Fig. 1**). This proves that  $\text{MHy}^+$  can stay in the final WBG perovskite films. The content of  $\text{MHy}$  in the annealed  $\text{MHy}$ -perovskite film was estimated by calculating the integrated area of the characteristic peak of  $^1\text{H}$  in  $\text{MHy}^+$  to that of  $\text{FA}^+$ . The calculated  $\text{MHy}^+/\text{FA}^+$  ratio was 6.8%, which is close to the ratio in the precursor solution (7.1%). Scanning electron microscopy (SEM) images show that the introduction of 5%  $\text{MHy}^+$  did not notably change the surface morphology of WBG perovskite films (**Supplementary Fig. 2**). To check whether  $\text{MHy}^+$  can enter the lattice and assess the dimensionalities of  $\text{MHy}^+$  species, we

performed the X-ray diffraction (XRD) measurements on WBG perovskite films with varying  $\text{MHy}^+$  substitution ratios from 0 to 20%. As shown in **Supplementary Fig. 3**, the substitution of  $\text{FA}^+$  by  $\text{MHy}^+$  resulted in a shift of XRD peaks towards smaller diffraction angles, leading to an expansion of the lattice constant in all crystallographic directions. Furthermore, we did not detect any diffraction peaks at small angles that belong to  $\text{MHy}^+$ -based 2D perovskite even when  $\text{MHy}^+$  was increased to 20%.

We performed density functional theory (DFT) calculations to explore the role of  $\text{MHy}^+$  on structural and electronic properties of WBG perovskites. Since halide migration has been often reported to have a smaller activation energy than A-cation migration,<sup>37</sup> we focused on halide migration in this study. We first calculated the migration energy barrier of iodide interstitial ( $\text{I}_i$ ) in  $\text{Cs}_{0.25}\text{FA}_{0.75}\text{PbI}_3$ , under two scenarios. In both scenarios,  $\text{MHy}^+$  replacing  $\text{Cs}^+$  and  $\text{FA}^+$  were examined (**Supplementary Fig. 4**). The simulations were based on the nudged elastic band (NEB) method to calculate the migration barriers of  $\text{I}_i$  by considering  $\text{I}_i$  migrating from initial position to the adjacent lattice site along the shortest path in the (110) direction (see the migration pathways in **Fig. 1**). The DFT results reveal that  $\text{MHy}^+$ -substituted perovskite exhibits a higher migration barrier (0.76 eV) for iodide ions traveling via an interstitial site when 5% of either  $\text{Cs}^+$  or  $\text{FA}^+$  is replaced by  $\text{MHy}^+$  (0.58 eV and 0.68 eV, **Fig. 1c-d** and **Supplementary Fig. 5**). This suggests that the inclusion of  $\text{MHy}^+$  can suppress  $\text{I}_i$  migration, likely due to lattice distortion, as compared to  $\text{Cs}^+/\text{FA}^+$ . The local lattice distortion, whether due to the size mismatch of A-site cations or the formation of Pb-N coordination bonds, may be responsible for the increased migration energy barrier<sup>36,38,39</sup>. It is worth noting that, while our DFT calculations offer some insights into the increased migration energy barrier associated with lattice distortions, they may not fully capture the complex, dynamic processes involved, such as the continuous formation of new interstitials

under illumination and the diverse redox reactions involving iodide species. Furthermore,  $\text{MHy}^+$  contains a strong reducing function group, which has been demonstrated to effectively reduce the detrimental  $\text{I}_2$  to  $\text{I}^-$ .<sup>40</sup> Iodine generation can occur in both precursor and perovskite over aging. A transparent FAI solution turned into light yellow when heated at 60 °C for two hours in ambient air conditions, indicating the formation of  $\text{I}_2$  by oxidization. To test the reducing capability of  $\text{MHy}^+$ , we introduced  $\text{MHyI}$  into the oxidized FAI solution at a 1% weight ratio. Upon the addition of  $\text{MHyI}$ , the solution became transparent, demonstrating the effectiveness of  $\text{MHy}^+$  in reducing  $\text{I}_2$  to  $\text{I}^-$  (**Supplementary Fig. 6**).<sup>41</sup> Similar strategies, such as using dimethylammonium formate (DMAFo) as an additive, have also been adopted to inhibit iodide oxidation in air-processed perovskite solar cells.<sup>41</sup> But the primary contribution of DMAFo is the enhancement of perovskite precursor stability.

We then carried out several measurements to investigate the photostability of WBG perovskite films with and without  $\text{MHy}^+$ . **Fig.2a-b** show the photoluminescence (PL) spectra of encapsulated  $\text{Cs}_{0.25}\text{FA}_{0.75}\text{Pb}(\text{I}_{0.82}\text{Br}_{0.15}\text{Cl}_{0.03})_3$  and  $\text{MHy}_{0.05}\text{Cs}_{0.25}\text{FA}_{0.7}\text{Pb}(\text{I}_{0.82}\text{Br}_{0.15}\text{Cl}_{0.03})_3$  perovskite films after aging under continuous 1-sun illumination for different durations up to 500 hours. The  $\text{Cs}_{0.25}\text{FA}_{0.75}\text{Pb}(\text{I}_{0.82}\text{Br}_{0.15}\text{Cl}_{0.03})_3$  perovskite film showed an obvious PL redshift, and full width at half maximum (FWHM) of PL peak became larger with increasing aging duration, suggesting the emerging of the photo-induced film degradation (**Fig. 2c**). In contrast, the  $\text{MHy}_{0.05}\text{Cs}_{0.25}\text{FA}_{0.7}\text{Pb}(\text{I}_{0.82}\text{Br}_{0.15}\text{Cl}_{0.03})_3$  perovskite film showed no PL peak shifting or broadening. A photoelectrochemical model has been developed by Kerner et al., which rationalizes that iodide oxidation is the first step of mixed halide segregation<sup>28,42</sup>. To elucidate the role of  $\text{MHy}^+$  in preventing iodide oxidation, we tracked the formation of  $\text{I}_2$  in WBG perovskite films by immersing the films in toluene at 65 °C when the films were illuminated for 500 h under continuous light at

1 sun intensity. We then measured the absorption spectra of the toluene solution to evaluate the released  $I_2$  during the aging. As shown in **Fig. 2d**, ultraviolet-visible (UV-vis) absorption measurements show that the toluene solution with aged control WBG perovskite film has a distinct absorption peak at 360 nm, which is assigned to  $I_2$ . By contrast, the  $MHy^+$ -incorporated perovskite film did not generate  $I_2$  after long-time illumination at high temperature, proving that  $MHy^+$  can inhibit iodide oxidation. Therefore, employing the  $MHy^+$  cation can facilitate efficient reduction of iodine not only in the solution state but also in the film state since it can be incorporated into perovskite lattice.

To verify the increased iodide migration energy barrier due to  $MHy^+$  substitution from DFT calculation, we measured the temperature-dependent conductivity to determine the activation energy ( $E_a$ ) of ion migration. Based on the Arrhenius plot shown in **Fig. 2e**, we derived  $E_a$  values of 0.43 eV and 0.81 eV for control and  $MHy^+$  WBG perovskite films, respectively, which are in alignment with the DFT calculation results. We further estimated the concentration of mobile ions using a mobile ion charging–discharging method. The typical transient currents in devices are shown in **Fig. 2f**. The calculated mobile ion concentrations decrease from  $4.2 \times 10^{15} \text{ cm}^{-3}$  for the control WBG device to  $2.4 \times 10^{15} \text{ cm}^{-3}$  for  $MHy^+$  device<sup>43</sup>. The mobile ion concentration in the  $MHy^+$  device is approximately two times lower than that in the control device, as the result of improved crystallinity after  $MHy^+$  incorporation<sup>44</sup>. The reduced mobile ion concentration together with the increased ion migration activation energy are beneficial for suppressing phase segregation.<sup>38</sup> Overall, the mechanism of suppressed phase segregation in  $MHy^+$ -incorporated WBG perovskites is attributed to two key factors. The first is the potential of the reductive  $MHy^+$  cation to prevent halide oxidation, which in turn slows down the phase segregation process. The halide oxidation has suggested to initiate the phase segregation process.<sup>28</sup> The second factor is

associated with the increased migration energy barrier of iodide species induced by the lattice distortion, thereby mitigating the phase segregation of WBG perovskite during operation.

### Optoelectronic properties of films and devices

We extended our DFT calculations to examine surface passivation by  $\text{MHy}^+$ , focusing on two representative perovskite surfaces (*i.e.*, FAI- and  $\text{PbI}_2$ -rich). As illustrated in **Supplementary Fig. 7**, for the FAI-rich surface, the replacement of surface  $\text{FA}^+$  with  $\text{MHy}^+$  enhances the binding energy of A-site cation with perovskite from  $-4.93$  eV to  $-5.14$  eV; and for the  $\text{PbI}_2$ -rich surface, the  $\text{MHy}^+$  ions passivate the undercoordinated  $\text{Pb}^{2+}$  ions at the surface through the formation of Pb–N coordination bonds. In the perovskite bulk, the  $\text{MHy}^+$  replacement can suppress the formation of iodide interstitials, as evident by the increased formation energy of iodide interstitials compared to the control case under the moderate growth condition ( $1.47$  eV vs  $1.10$  eV, **Supplementary Fig. 8**). Therefore,  $\text{MHy}^+$  ions play a dual role in reducing defect densities within perovskites and enabling higher activation energy for iodide migration, underscoring its significance in enhancing WBG perovskite device stability and efficiency.

To have a better insight into the effects of  $\text{MHy}^+$  on the optoelectronic properties of WBG perovskite films and devices, we performed various measurements. To evaluate the passivation effect of  $\text{MHy}^+$ , we studied the charge carrier recombination kinetics of the 5%  $\text{MHy}^+$ -substituted  $\text{MHy}_{0.05}\text{Cs}_{0.25}\text{FA}_{0.7}\text{Pb}(\text{I}_{0.82}\text{Br}_{0.15}\text{Cl}_{0.03})_3$  and the control WBG perovskite films via time-resolved photoluminescence (TRPL) spectroscopy. As shown in **Fig. 3a**, the measured carrier recombination lifetimes are  $534$  ns and  $163$  ns for 5%  $\text{MHy}^+$ -substituted  $\text{MHy}_{0.05}\text{Cs}_{0.25}\text{FA}_{0.7}\text{Pb}(\text{I}_{0.82}\text{Br}_{0.15}\text{Cl}_{0.03})_3$  and control samples, respectively, showing that  $\text{MHy}^+$  substitution can effectively suppress the nonradiative recombination. Confocal PL intensity and PL lifetime mapping were used to further understand the charge carrier dynamics uniformity in

WBG perovskite films (**Fig. 3b-c**). The  $\text{MHy}^+$  perovskite film shows uniformly enhanced PL intensity and recombination lifetime.

We also investigated the charge carrier dynamics in WBG PSCs. As shown in **Fig. 3d**, electroluminescence (EL) spectra of the control and  $\text{MHy}^+$  devices were recorded at an injection current of  $21 \text{ mA/cm}^2$  (close to device's  $J_{\text{SC}}$  value). The  $\text{MHy}^+$  device shows a 3.8-fold higher EL intensity than the control device, which is expected to increase the  $V_{\text{OC}}$  by  $\sim 35 \text{ mV}$ . We then measured transient photovoltage (TPV), and trap density state (tDOS) of control and  $\text{MHy}^+$  devices. The TPV was conducted with a light bias of 1 sun light intensity which made the devices operate at  $V_{\text{OC}}$  condition for both control and target devices. This was evidenced by the observed  $V_{\text{OC}}$  of  $1.27 \text{ V}$  for the  $\text{MHy}^+$  device and  $1.23 \text{ V}$  for the control device. A perturbation of carrier concentration was induced by a weak nanosecond pulse laser, and the decay of the perturbation carrier density has a lifetime of  $0.76 \mu\text{s}$  in the  $\text{MHy}^+$  device and  $0.48 \mu\text{s}$  in the control device (**Fig. 3e**), directly confirmed the slower recombination in the device with  $\text{MHy}^+$ . To find out the origin of longer carrier recombination lifetime, we characterized the defect density in the devices using thermal admittance spectroscopy. The  $\text{MHy}^+$  device exhibits a lower trap density in the trap depth region from  $0.25$  to  $0.40 \text{ eV}$  characterized by thermal admittance spectroscopy (**Fig. 3f**). The observed trap bands are associated with positive and negative iodide interstitials<sup>21,45</sup>, agreeing with the computation results that big size  $\text{MHy}^+$  incorporation can reduce iodide interstitial formation. The densities of both negatively charged iodide interstitial ( $\text{I}_i^-$ ) and positively charged iodide interstitial ( $\text{I}_i^+$ ) are reduced. Hole trapping at iodide sites, such as negative  $\text{I}_i^-$ , has been proposed to induce lattice instability and halide phase segregation in mixed halide perovskites.<sup>46</sup> Our previous result shows that reducing the concentration of  $\text{I}_i^+$  defect will suppress energy loss for

WBG devices.<sup>7,21</sup> Therefore, the simultaneous reduction for the concentration of  $I_i^+$  and  $I_i^-$  is crucial to achieve high efficiency and stability WBG perovskite solar cells.

### Device performance and module development

We first investigated the performance of blade-coated small-area WBG PSCs with a structure of ITO/Meo-2PACz/PTAA/MHy<sub>1-x-y</sub>Cs<sub>x</sub>FA<sub>y</sub>Pb(I<sub>0.82</sub>Br<sub>0.15</sub>Cl<sub>0.03</sub>)<sub>3</sub>/C<sub>60</sub>/BCP/Cu, where ITO is indium tin oxide, Meo-2PACZ is [2-(3,6-dimethoxy-9H-carbazol-9-yl)ethyl]phosphonic acid, PTAA is poly[bis(4-phenyl)(2,4,6-trimethylphenyl)amine], and BCP is bathocuproine. The *J-V* curves of WBG PSCs with various MHy<sup>+</sup> ratio was shown in **Supplementary Fig. 9**. The 5% MHy<sup>+</sup> content in precursor solution was found to be optimal. As shown **Fig. 4a**, the champion MHy<sup>+</sup> PSC (aperture area of 0.08 cm<sup>2</sup>) had a PCE of 23.3% with a short-circuit current density ( $J_{SC}$ ) of 21.8 mA cm<sup>-2</sup>, a  $V_{OC}$  of 1.28 V, and a fill factor (FF) of 0.838, significantly outperforming the control WBG PSCs (PCE=21.6%,  $J_{SC}$ =21.7 mA cm<sup>-2</sup>,  $V_{OC}$ =1.23 V, FF=0.810). Both control and MHy<sup>+</sup> devices exhibited negligible photocurrent hysteresis. The stabilized power outputs of best-performing control and MHy<sup>+</sup> devices were measured and shown in **Fig. 4b**. The stabilized PCEs for control and MHy<sup>+</sup> PSCs were 21.6 and 23.2%, respectively. As shown in **Supplementary Fig. 10**, the efficiency of our champion device is the highest reported of all WBG PSCs (band gaps ranging from 1.65 to 1.68 eV). The  $V_{OC}$  deficit of the best-performing MHy<sup>+</sup> WBG PSC was only 0.37 V, considering the 1.65 eV-bandgap of the perovskite films derived from the external quantum efficiency (EQE) curves. To the best of our knowledge, the  $V_{OC}$  deficit of 0.37 V is the lowest value reported for WBG PSCs. The corresponding EQE spectra of the devices are shown in **Fig. 4c**. The integrated current densities are in good agreement with  $J_{SC}$  extracted from *J-V* curves. The statistical distributions of photovoltaic parameters for WBG PSCs across 30 devices are shown in **Fig. 4d**. The average values for  $V_{OC}$  and FF and PCE are higher in MHy<sup>+</sup>

PSCs. The primary enhancement in device efficiency can be attributed to the increased FF and  $V_{OC}$ , originating from reduced charge recombination and prolonged carrier lifetime. We further investigated the long-term operational stability of encapsulated WBG PSCs under 1 sun illumination. No temperature controlled was applied, so the temperature of the devices was increased to  $55\pm 5$  °C by the illumination light. The encapsulated MHy<sup>+</sup> WBG PSCs demonstrated a remarkably low PCE reduction of less than 5% after 800 hours, representing one of the best reported stabilities for WBG PSCs (Table S1). In contrast, the control device exhibited approximately 20% loss within the same timeframe (**Fig. 4e**).

We evaluated whether this composition can be upscaled by fabricating WBG perovskite modules using the blade coating process in ambient conditions. **Fig. 5a** shows a photograph of an encapsulated WBG perovskite minimodule with an aperture area of 25 cm<sup>2</sup>. The subcell width for WBG perovskite module was 6.5 mm. A high geometric FF of 96% was achieved with a narrow dead area width of 270 μm (**Fig. 5a**). We fabricated multiple MHy<sup>+</sup> WBG perovskite minimodules, which showed an average PCE of  $18.4\pm 0.8\%$  (**Supplementary Fig. 11**). The best-performing MHy<sup>+</sup> WBG perovskite minimodule exhibited an aperture PCE of 19.9%, with a  $V_{OC}$  of 8.89 V, short-circuit current ( $I_{SC}$ ) of 73.94 mA, and a FF of 0.757 (**Fig. 5b**). It is notable that each subcell has a  $V_{OC}$  of 1.27 V from the minimodule, showing the good reproducibility of the composition. The stabilized minimodule aperture PCE is 19.8% at a bias voltage of 6.7 V, as shown in **Fig. 5c**. The operational stability of a MHy<sup>+</sup> WBG perovskite minimodule was also tested. **Fig. 5d** shows the evolution of PCE of an encapsulated WBG perovskite module under 1 sun illumination under  $V_{OC}$  condition in ambient air. The encapsulated WBG perovskite minimodule maintained 94% of the initial PCE after 700 h of operation under continuous 1 sun illumination ( $55\pm 5$  °C). **Fig. 5e** shows the  $I$ - $V$  curves of WBG perovskite minimodules after operational testing for different

durations. The PL spectra of the WBG perovskite minimodules were recorded before and after operational stability test (**Supplementary Fig. 12**), which showed no obvious change in terms of PL peak shift and broadening.

## **Discussion**

In summary, we have successfully demonstrated that the reductive A-site cation  $\text{MHy}^+$  can be incorporated into WBG perovskites, improving both efficiency and stability of WBG perovskite devices. The reductive  $\text{MHy}^+$  can inhibit the halide oxidation and provide high diffusion barrier for the migration of halide species, which significantly suppresses the halide segregation of WBG perovskites, thus improving the operational stability. We found that  $\text{MHy}^+$  can provide uniform passivation to perovskite films, enabling a  $V_{\text{OC}}$  of 1.28 V for WBG perovskite with a bandgap of 1.65 eV, which is 93.4% of the Shockley-Queisser limit  $V_{\text{OC}}$  (1.37 V). In addition, we have demonstrated the scalable fabrication of high-performance of WBG perovskite modules in ambient air conditions, achieving a champion module efficiency of 19.9% with an aperture area of 25 cm<sup>2</sup> along with good long-term operational stability. By providing a viable pathway for the large-scale deployment of high-performance solar modules in ambient air, our work supports the transition to clean energy sources, helping to reduce greenhouse gas emissions and promote environmental sustainability.

## Methods

Lead(II) iodide ( $\text{PbI}_2$ , 99.99% trace metals basis, TCI), Formamidinium iodide (FAI, 99.99%, GreatCell Solar), 4-fluoro-phenethylammonium iodide (4-F-PEAI, >99%, GreatCell Solar), L- $\alpha$ -phosphatidylcholine (LP,  $\geq 99\%$ , Sigma-Aldrich), 5%v/v  $\text{FAH}_2\text{PO}_2$  (synthesized in our lab), dodecylammonium iodide (GreatCell Solar), lead bromide ( $\text{PbBr}_2$ ), caesium iodide (CsI), BCP, dimethyl sulfoxide, N, N-Dimethylformamide (DMF), isopropanol (IPA), bathocuproine (BCP), 2-methoxyethanol (2-ME) and toluene were purchased from Sigma-Aldrich, N-methyl-2-pyrrolidone (NMP, 99.9%, Sigma-Aldrich),  $\text{TPABr}_3$  (TCI),  $\text{C}_{60}$  was purchased from NANO-C company, Copper (Cu) pellets were purchased from Kurt J. Lesker Company.

Synthesis of Methylhydrazine iodide (MHyI): 2.63 mL of methylhydrazine solution was diluted with 5 mL of anhydrous IPA and stirred with an ice bath. Then 100 mL of HI solution was added to the above solution. The reaction was stirred for a further 2 h and then worked up by evaporation of the solvent. The white precipitate was recrystallized and washed 2-3 times with ethanol and diethyl ether. The white MHyI powder obtained was dried in a vacuum oven at 60 °C. The MHyI powder was dried in a vacuum oven at 60 °C.

### Device fabrication

Patterned ITO glass was cleaned with acetone and isopropanol using ultrasonic cleaning for 15 minutes, followed by 15 minutes of ultraviolet ozone treatment. The double hole transport layers were sequentially blade coated on ITO substrates by using  $0.5 \text{ mg mL}^{-1}$  Meo-2PACz in methanol and  $2.2 \text{ mg mL}^{-1}$  PTAA in toluene with a 200  $\mu\text{m}$  blade gap (same coating speed of 20 mm/s). In detail, Meo-2PACz was first blade-coated on ITO substrate and then annealed at 100 °C for 5 min and washed by methanol to remove the residue molecule. PTAA layer was then blade-

coated onto the Meo-2PACz-coated ITO substrate. To blade-coat  $\text{MHy}_x\text{Cs}_{0.25}\text{FA}_{0.7-x}\text{Pb}(\text{I}_{0.82}\text{Br}_{0.15}\text{Cl}_{0.3})_3$  WBG perovskite films, 1.4 M  $\text{MHy}_x\text{Cs}_{0.25}\text{FA}_{0.7-x}\text{Pb}(\text{I}_{0.82}\text{Br}_{0.15}\text{Cl}_{0.3})_3$  ink solution was dissolved in DMF with  $\text{FAH}_2\text{PO}_2$  (0.15 wt%), LP (0.05 wt%, LP was dissolved in 2-methoxyethanol), n-octylammonium iodide (0.1 wt%), phenylethylammonium chloride (0.05 wt%),  $\text{TPABr}_3$  (0.1 mol%) and 20 mol% of NMP (compared with lead), and then blade coated onto a PTAA/Meo-2PACz-coated ITO substrate using an  $\text{N}_2$  knife (20 psi) at a coating speed of  $20 \text{ mms}^{-1}$  and coating gap of  $250 \mu\text{m}$ . The as-coated solid perovskite films were then annealed at  $70^\circ\text{C}$  for 10 min and followed by annealing at  $100^\circ\text{C}$  for another 3 min in air. Then 30 nm of  $\text{C}_{60}$ , 6 nm of BCP and 80 nm of copper were sequentially deposited by thermal evaporation. The minimodules were fabricated on pre-patterned large ITO glass substrates with P1 width of  $30 \mu\text{m}$  followed by the same procedure as the small solar cells. The laser scribing was performed twice with a Keyence laser marker (MD-U1000C, 355 nm). The width of each subcell is 6.5 mm, while the final P2 and P3 widths were measured to be  $\sim 80$  and  $\sim 60 \mu\text{m}$ , respectively. The total width of the non-working area was measured to be  $\sim 250 \mu\text{m}$ , giving a GFF of 94.7%. A polydimethylsiloxane (PDMS) layer was attached to the front side of the perovskite solar cells as an anti-reflection coating.

#### Device characterization

The  $J-V$  characteristics of solar cells and modules were measured using a Keithley 2400 source meter under the simulated AM 1.5 G 1 sun illumination ( $100 \text{ mW cm}^{-2}$ ) using a solar simulator (Oriol Sol 3 A class AAA) equipped with 450 W Xenon lamp (Newport 6280NS). The light intensity was calibrated using a Si solar cell with a KG-5 filter. The active area of devices is  $0.08 \text{ cm}^2$ , defined by the size of the Cu electrode. The devices were measured at ambient air with humidity of 30–60% without temperature control. The scan rate during measurement was set to

50 mV s<sup>-1</sup>. Steady-state PCE was conducted by measuring stabilized photocurrent density under a constant bias voltage at maximum power point derived from  $J-V$  curves. An anti-reflection coating was used during measurement. A Newport QE measurement kit was used to measure the External quantum efficiency spectra of PSCs. A monochromatic light beam from a Xenon Arc lamp coupled with a Bruker Vertex 80 v Fourier Transform Interferometer was incident and focused onto the devices. Then, the photocurrent was obtained through a Stanford Research SR570 current pre-amplifier. EQE devices was calibrated by a Newport reference silicon solar cell with a known EQE. Transient photovoltage decays were measured under 1 sun illumination with a 337 nm laser pulse (SRS NL 100 Nitrogen Laser, pulse duration of less than 3.5 ns) to add a small perturbation to the background illumination. The voltage of the device was measured with a digital oscilloscope (DOS-X 3104 A) with an input impedance set to 1 M $\Omega$ . The trap density of state of solar cells was derived from the frequency-dependent capacitance and voltage-dependent capacitance according to our previous study<sup>45</sup>. Time-resolved photoluminescence (TRPL) spectroscopy was conducted on a DeltaFlex modular fluorescence lifetime system from Horiba Scientific with a pulsed laser source at 406 nm (Horiba NanoLED 402-LH; pulse width below 200 ps, 20 pJ per pulse,  $\sim$ 1 mm<sup>2</sup> spot size) with a repetition rate of 0.3125 MHz. Mobile ion concentration measurement can be found in our previous work<sup>44</sup>.

#### Device encapsulation and stability evaluation

Small-area PSCs were encapsulated by cover glasses sealed with epoxy encapsulant (Devcon 14250). In this process, the epoxy encapsulant is sandwiched between Cu-electrodes and cover glasses to protect all the layers while the electrodes are sticking out. Perovskite modules were encapsulated by polyisobutylene (PIB, HelioSeal PVS 101) blanket with a laminator (LAB-LAMINATOR L036LAB) at 110 °C for 10 min. PIB blanket, which means the device was fully

covered by the PIB and then sandwiched between the device substrate glass and cover glass. A LED lamp (SOLLA, IP66, 600W) with a light intensity equivalent to AM 1.5 G worked as a solar simulator in the air (relative humidity,  $\sim 50 \pm 10\%$ ). The Spectrum of LED lamp was provided in Supplementary Figure 13. Devices were tested under open-circuit (OC) conditions and without any resistance load. The temperature of the solar cells was measured to be  $55 \pm 5^\circ\text{C}$  due to the heating effects of the lamp. The device efficiency was measured at different times, and device temperature and relative humidity were recorded simultaneously.

### DFT calculations

Density functional theory (DFT) calculations were carried out using the projector-augmented wave (PAW) method as implemented in the Vienna Ab initio Simulation Package (VASP) code. The generalized gradient approximation (GGA) with the Perdew-Burke-Ernzerhof (PBE) exchange-correlation functional was used. A uniform  $2 \times 2 \times 2$   $k$ -mesh grid in the Brillouin zone was employed to optimize the crystal structure of  $3 \times 3 \times 3$  supercells  $\text{Cs}_{0.3}\text{FA}_{0.7}\text{PbI}_3$  (Cs:FA = 8:19),  $\text{Cs}_{0.25}\text{FA}_{0.75}\text{PbI}_3$  (Cs:FA = 7:20), and  $\text{MHy}_{0.05}\text{Cs}_{0.25}\text{FA}_{0.7}\text{PbI}_3$  (MHy:Cs:FA = 1:7:19), and a  $2 \times 2 \times 1$   $k$ -mesh was used for their slabs. The  $\text{Cs}_{0.25}\text{FA}_{0.75}\text{PbI}_3$  and  $\text{MHy}_{0.05}\text{Cs}_{0.25}\text{FA}_{0.7}\text{PbI}_3$  slab models had a  $(2 \times 2)$  lateral periodicity with exposed (100) surface and the slab replica was separated by  $\sim 20$  Å of vacuum. The plane-wave basis set cutoff of the wave functions was set at 400 eV for the supercells and slabs. The atomic positions of all structures were fully relaxed until the supercells had forces on each atom less than  $0.015 \text{ eV}/\text{Å}$ . The migration of iodine ions was examined by using the nudged elastic band (NEB) method and constrained energy minimization techniques. The energy barriers for iodine ion migration were calculated by taking the differences between the total energy of the ground state for the perovskite supercells under consideration and the energies at the saddle points along the diffusion pathway.

## Data availability

The data that support the findings of this study are available within the Article and its Supplementary Information file. Source data are provided with this paper.

## References

- 1 Zhou, J. *et al.* Highly efficient and stable perovskite solar cells via a multifunctional hole transporting material. *Joule* **8**, 1691-1706 (2024).
- 2 Chen, H. *et al.* Improved charge extraction in inverted perovskite solar cells with dual-site-binding ligands. *Science* **384**, 189-193 (2024).
- 3 Park, N.-G., Grätzel, M., Miyasaka, T., Zhu, K. & Emery, K. Towards stable and commercially available perovskite solar cells. *Nat. Energy* **1**, 1-8 (2016).
- 4 Meng, L., You, J. & Yang, Y. Addressing the stability issue of perovskite solar cells for commercial applications. *Nat. Commun.* **9**, 5265 (2018).
- 5 Park, N.-G. & Zhu, K. Scalable fabrication and coating methods for perovskite solar cells and solar modules. *Nat. Rev. Mater.* **5**, 333-350 (2020).
- 6 Rong, Y. *et al.* Challenges for commercializing perovskite solar cells. *Science* **361**, eaat8235 (2018).
- 7 Fei, C. *et al.* Lead-chelating hole-transport layers for efficient and stable perovskite minimodules. *Science* **380**, 823-829 (2023).
- 8 Tan, Q. *et al.* Inverted perovskite solar cells using dimethylacridine-based dopants. *Nature* **620**, 545-551 (2023).
- 9 Zhang, S. *et al.* Minimizing buried interfacial defects for efficient inverted perovskite solar cells. *Science* **380**, 404-409 (2023).
- 10 Jiang, Q. *et al.* Surface reaction for efficient and stable inverted perovskite solar cells. *Nature* **611**, 278-283 (2022).
- 11 Jeong, M. *et al.* Stable perovskite solar cells with efficiency exceeding 24.8% and 0.3-V voltage loss. *Science* **369**, 1615-1620 (2020).
- 12 Chen, S. *et al.* Stabilizing perovskite-substrate interfaces for high-performance perovskite modules. *Science* **373**, 902-907 (2021).
- 13 Ding, B. *et al.* Dopant-additive synergism enhances perovskite solar modules. *Nature* **628**, 299-305 (2024).
- 14 Weerasinghe, H. C. *et al.* The first demonstration of entirely roll-to-roll fabricated perovskite solar cell modules under ambient room conditions. *Nat. Commun.* **15**, 1656 (2024).
- 15 Yang, Y. *et al.* A thermotropic liquid crystal enables efficient and stable perovskite solar modules. *Nat. Energy* **9**, 316-323 (2024).
- 16 Yang, G. *et al.* Stable and low-photovoltage-loss perovskite solar cells by multifunctional passivation. *Nat. Photonics* **15**, 681-689 (2021).

- 17 Aydin, E. *et al.* Pathways toward commercial perovskite/silicon tandem photovoltaics. *Science* **383**, eadh3849 (2024).
- 18 Aydin, E. *et al.* Enhanced optoelectronic coupling for perovskite/silicon tandem solar cells. *Nature* **623**, 732-738 (2023).
- 19 Mariotti, S. *et al.* Interface engineering for high-performance, triple-halide perovskite–silicon tandem solar cells. *Science* **381**, 63-69 (2023).
- 20 Al-Ashouri, A. *et al.* Monolithic perovskite/silicon tandem solar cell with > 29% efficiency by enhanced hole extraction. *Science* **370**, 1300-1309 (2020).
- 21 Yang, G. *et al.* Defect engineering in wide-bandgap perovskites for efficient perovskite–silicon tandem solar cells. *Nat. Photonics* **16**, 588-594 (2022).
- 22 Wright, M. *et al.* Design considerations for the bottom cell in perovskite/silicon tandems: a terawatt scalability perspective. *Energy Environ. Sci.* **16**, 4164-4190 (2023).
- 23 Yang, G. *et al.* Shunt mitigation toward efficient large-area perovskite-silicon tandem solar cells. *Cell Rep. Phys. Sci.* **4**, 101628 (2023).
- 24 Xu, K. *et al.* Slot-die coated triple-halide perovskites for efficient and scalable perovskite/silicon tandem solar cells. *ACS Energy Lett.* **7**, 3600-3611 (2022).
- 25 Chen, B. *et al.* Blade-coated perovskites on textured silicon for 26%-efficient monolithic perovskite/silicon tandem solar cells. *Joule* **4**, 850-864 (2020).
- 26 Ramadan, A. J., Oliver, R. D., Johnston, M. B. & Snaith, H. J. Methylammonium-free wide-bandgap metal halide perovskites for tandem photovoltaics. *Nat. Rev. Mater.* **8**, 822-838 (2023).
- 27 Wang, X. *et al.* Perovskite solution aging: what happened and how to inhibit? *Chem* **6**, 1369-1378 (2020).
- 28 Kerner, R. A., Xu, Z., Larson, B. W. & Rand, B. P. The role of halide oxidation in perovskite halide phase separation. *Joule* **5**, 2273-2295 (2021).
- 29 Duan, L. *et al.* Stability challenges for the commercialization of perovskite–silicon tandem solar cells. *Nat. Rev. Mater.* **8**, 261-281 (2023).
- 30 Xu, J. *et al.* Triple-halide wide-band gap perovskites with suppressed phase segregation for efficient tandems. *Science* **367**, 1097-1104 (2020).
- 31 Mączka, M. a. *et al.* Methylhydrazinium lead bromide: noncentrosymmetric three-dimensional perovskite with exceptionally large framework distortion and green photoluminescence. *Chem. Mater.* **32**, 1667-1673 (2020).
- 32 Mączka, M. *et al.* [Methylhydrazinium]<sub>2</sub>PbBr<sub>4</sub>, a ferroelectric hybrid Organic–Inorganic Perovskite with multiple nonlinear optical outputs. *Chem. Mater.* **33**, 2331-2342 (2021).
- 33 Szafranski, M. Structural and optical properties of methylhydrazinium lead bromide perovskites under pressure. *J. Mater. Chem. A* **12**, 2391-2399 (2024).
- 34 Fedoruk, K. *et al.* [Methylhydrazinium]<sub>2</sub>PbCl<sub>4</sub>, a two-dimensional perovskite with polar and modulated phases. *Inorg. Chem.* **61**, 15520-15531 (2022).
- 35 Mączka, M. *et al.* Three-dimensional perovskite methylhydrazinium lead chloride with two polar phases and unusual second-harmonic generation bistability above room temperature. *Chem. Mater.* **32**, 4072-4082 (2020).
- 36 Mączka, M. *et al.* The lattice symmetrization worked, but with a plot twist: effects of methylhydrazinium doping of MAPbI<sub>3</sub> on phase transitions, cation dynamics and photoluminescence. *J Mater Chem C* **12**, 1396-1405 (2024).
- 37 Zai, H., Ma, Y., Chen, Q. & Zhou, H. Ion migration in halide perovskite solar cells: Mechanism, characterization, impact and suppression. *J. Energ. Chem.* **63**, 528-549 (2021).

- 38 Wang, Z. *et al.* Suppressed phase segregation for triple-junction perovskite solar cells. *Nature* **618**, 74-79 (2023).
- 39 Zhang, L. *et al.* Manipulating Local Lattice Distortion for Spectrally Stable and Efficient Mixed-halide Blue Perovskite LEDs. *Angew. Chem. Int. Ed.* **62**, e202302184 (2023).
- 40 Chen, S., Xiao, X., Gu, H. & Huang, J. Iodine reduction for reproducible and high-performance perovskite solar cells and modules. *Science Advances* **7**, eabe8130 (2021).
- 41 Meng, H. *et al.* Inhibition of halide oxidation and deprotonation of organic cations with dimethylammonium formate for air-processed p-i-n perovskite solar cells. *Nature Energy* **9**, 536-547 (2024).
- 42 Wu, S. *et al.* Redox mediator-stabilized wide-bandgap perovskites for monolithic perovskite-organic tandem solar cells. *Nature Energy* **9**, 411-421 (2024).
- 43 Bertoluzzi, L. *et al.* Mobile ion concentration measurement and open-access band diagram simulation platform for halide perovskite solar cells. *Joule* **4**, 109-127 (2020).
- 44 Wang, M. *et al.* Ammonium cations with high pK<sub>a</sub> in perovskite solar cells for improved high-temperature photostability. *Nat. Energy* **8**, 1229-1239 (2023).
- 45 Ni, Z. *et al.* Evolution of defects during the degradation of metal halide perovskite solar cells under reverse bias and illumination. *Nat. Energy* **7**, 65-73 (2022).
- 46 DuBose, J. T. & Kamat, P. V. Hole trapping in halide perovskites induces phase segregation. *Acc. Mater. Res.* **3**, 761-771 (2022).

## Acknowledgements

This work was mainly supported by the Solar Energy Technologies office within the US Department of Energy (DOE), Office of Energy Efficiency and Renewable Energy, under award number DE-EE0008749 and DE-EE0009520. We thank the financial support from National Science Foundation under award DMR-1903981. The views expressed in the article do not necessarily represent the views of the DOE or the U.S. Government. This work was performed in part at the Chapel Hill Analytical and Nanofabrication Laboratory, CHANL, a member of the North Carolina Research Triangle Nanotechnology Network, RTNN, which is supported by the National Science Foundation, Grant ECCS-2025064, as part of the National Nanotechnology Coordinated Infrastructure, NNCI.

## Author information

Authors and Affiliations

**Department of Applied Physical Sciences, The University of North Carolina at Chapel Hill,  
NC 27599, USA**

Guang Yang, Hangyu Gu, Jun Yin, Chengbin Fei, Zhifang Shi, Xiaoqiang Shi, Xingjian Ying,  
Jinsong Huang

**Department of Electrical and Electronic Engineering, Photonic Research Institute (PRI),  
Research Institute of Smart Energy (RISE), Research Institute for Advanced Manufacturing  
(RIAM), The Hong Kong Polytechnic University, Hung Hom, Kowloon, Hong Kong, China**

Guang Yang

**Department of Applied Physics, The Hong Kong Polytechnic University, Hung Hom,  
Kowloon, Hong Kong, China**

Jun Yin

**Department of Chemistry, The University of North Carolina at Chapel Hill Chapel Hill, NC  
27599, USA**

Jinsong Huang

Contributions

G.Y. and J.H. conceived the idea. G.Y. fabricated WBG perovskite solar cells and modules and conducted most of the characterizations and measurements of films and devices. J.Y. performed the DFT calculations. H.G., X.S., and C.F. did the laser scribing process. Z.S. synthesized MHyI. X.Y. optimized the blade coating parameters. G.Y. and J.H. wrote the paper, and all the authors reviewed the paper.

Corresponding authors

Jinsong Huang, email: [jhuang@unc.edu](mailto:jhuang@unc.edu)

### **Competing interests**

The authors declare no competing interests.

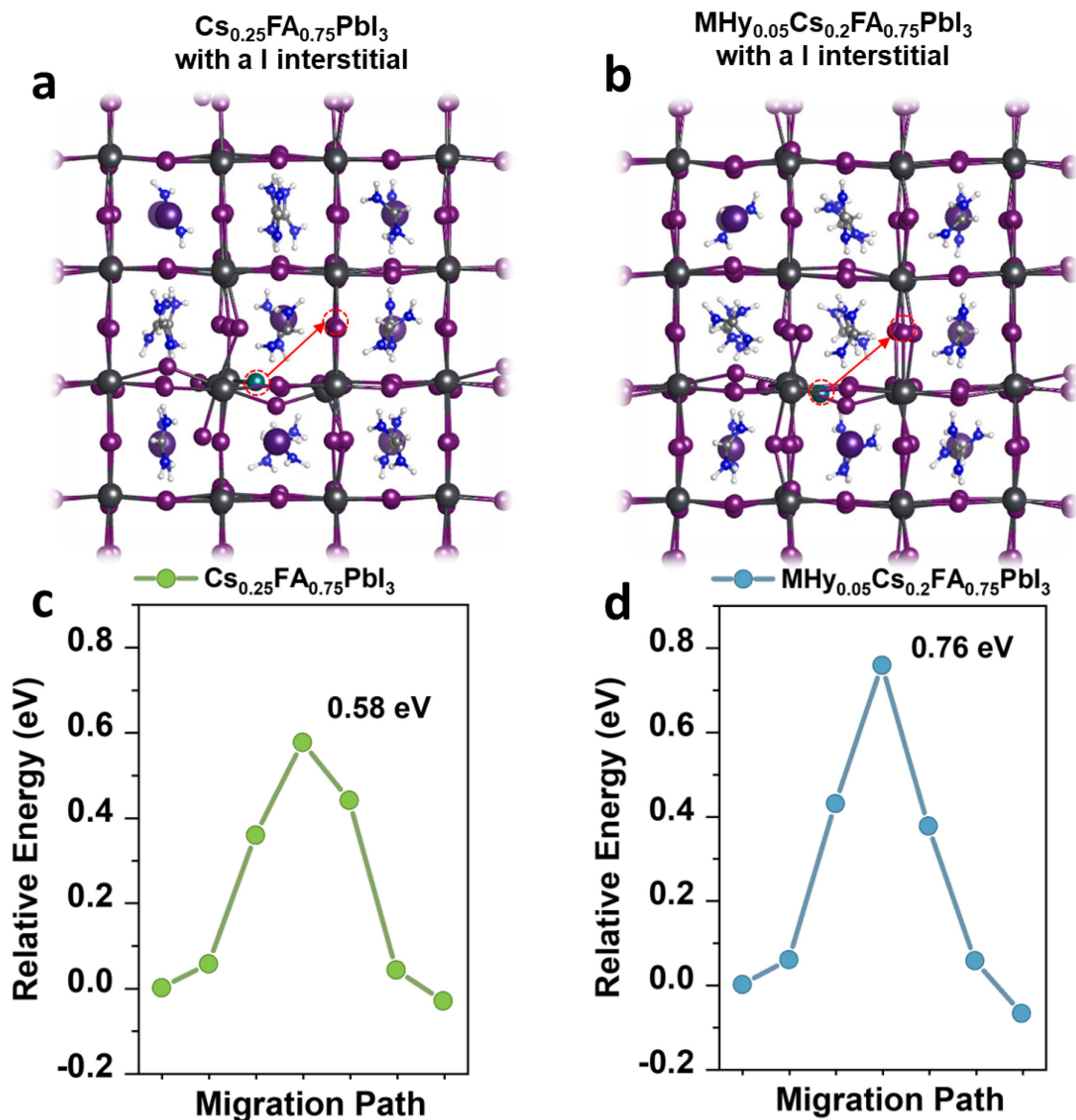


**Fig. 1.** DFT calculations of ion migration barrier. a,b, Crystal structures of  $\text{Cs}_{0.25}\text{FA}_{0.75}\text{PbI}_3$  and  $\text{MHy}_{0.05}\text{Cs}_{0.2}\text{FA}_{0.75}\text{PbI}_3$  with and without an I interstitial ( $\text{I}_i$ ). The red arrow represents the  $\text{I}_i$  migration pathways. c,d, Calculated relative activation energies for the  $\text{I}_i$  migration in  $\text{Cs}_{0.25}\text{FA}_{0.75}\text{PbI}_3$  and  $\text{MHy}_{0.05}\text{Cs}_{0.2}\text{FA}_{0.75}\text{PbI}_3$ . The MHy-substituted perovskite exhibits a higher energy barrier for  $\text{I}_i$  migration (0.76 eV) compared to  $\text{Cs}_{0.25}\text{FA}_{0.75}\text{PbI}_3$  (0.58 eV). The DFT calculations were performed at generalized gradient approximation (GGA)/Perdew–Burke–Ernzerh (PBE) theory level of theory.

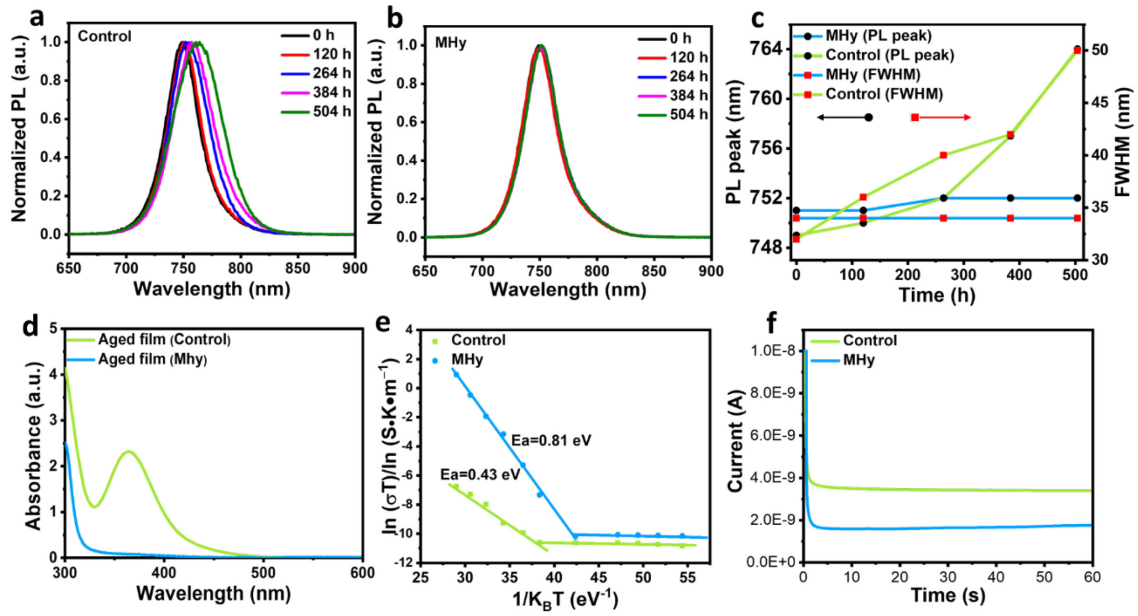


**Fig. 2. Suppressed phase halide segregation, ion migration, and inhibited halide oxidation. a,** **b,** Evolution of time-dependent PL spectra of control **(a)** and MHy<sup>+</sup> **(b)** WBG perovskite films under continuous light illumination. **c,** Time-dependent PL peak and full width at half maximum (FWHM) of PL. **d,** Absorbance spectra of toluene solutions in which WBG perovskite films were soaked at 65 °C for 500 hours. **e,** The temperature-dependent conductivity of the control and MHy<sup>+</sup> WBG perovskite films. **f,** Transient ion migration currents.

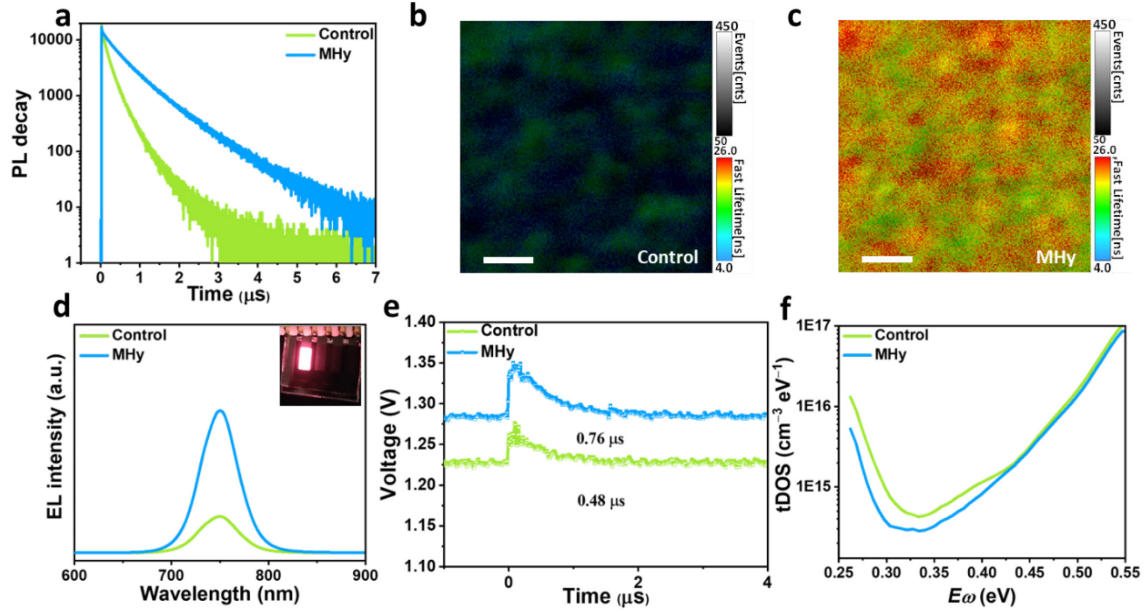


**Fig. 3. Characterizations of WBG perovskite films and devices.** **a**, Time-resolved PL decays of the WBG perovskite films with and without MHy<sup>+</sup> cation. **b**, **c**, Photoluminescence and lifetime mapping images of WBG perovskite films without (**b**) and with (**c**) MHy<sup>+</sup> cation. Scale bars, 2 μm. **d**, Electroluminescence spectra of perovskite devices with and without MHy<sup>+</sup>. The inset shows the picture of a MHy<sup>+</sup> WBG perovskite device operated under bias as a light-emitting diode (LED). **e**, Transient photovoltage response of the control and MHy<sup>+</sup> devices. **f**, tDOS curves of the control and MHy<sup>+</sup> devices.

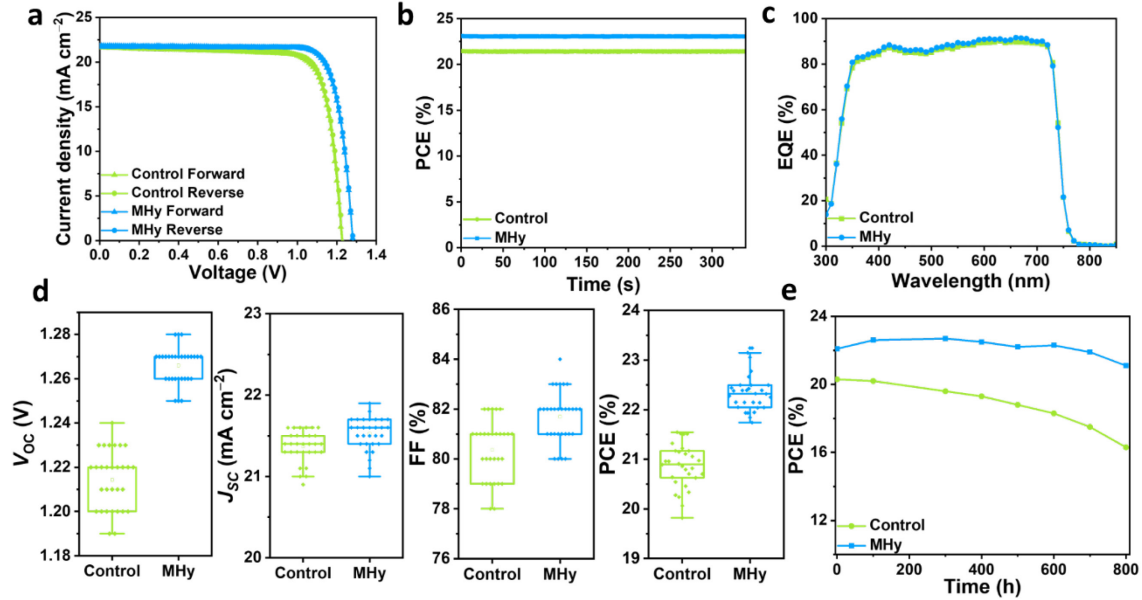


**Fig. 4. Efficiency and stability of small-area WBG PSCs.** **a**,  $J$ - $V$  curves, **b**, stabilized power output, **c**, EQE of control and MHy<sup>+</sup> WBG PSCs. **d**, Photovoltaic parameter statistics of the control and MHy<sup>+</sup> WBG PSCs with an aperture area of  $0.08 \text{ cm}^2$  from 60 devices and three individual batches. In the boxplots, whiskers: maxima and minima; bounds of box: 25th and 75th percentile; center: mean) are shown. **e**, Operational stability test of small-area control and MHy<sup>+</sup> PSCs.

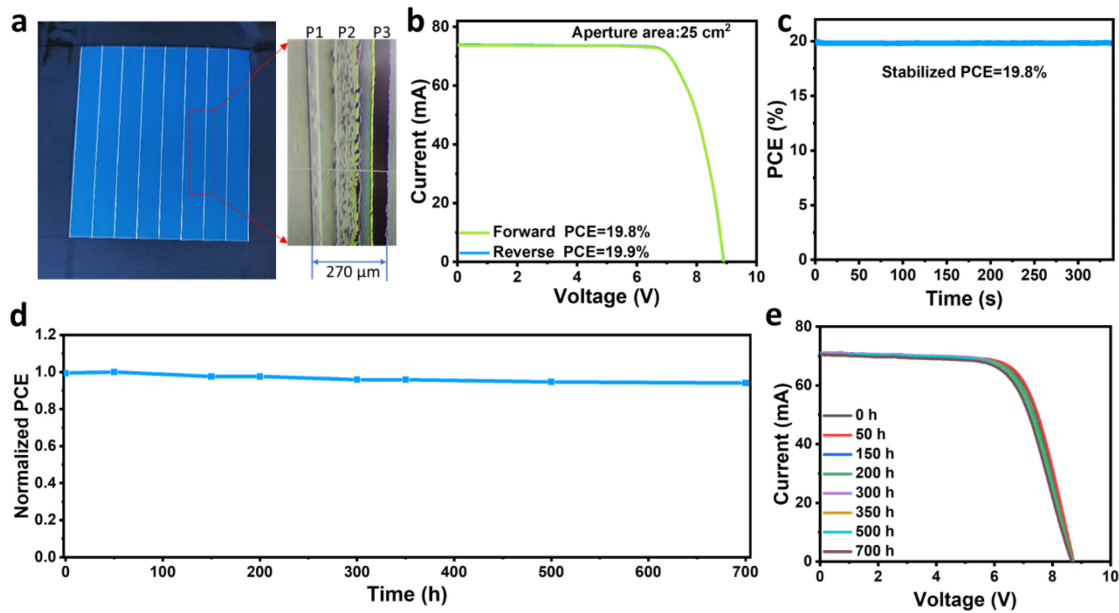


**Fig 5. Photovoltaic performance and stability of WBG perovskite modules.** **a**, A picture of WBG perovskite module (left) and a microscope image of all lines P1, P2 and P3. **b**, The  $I$ - $V$  curves of best-performing WBG perovskite module with an aperture area of 25 cm<sup>2</sup>. **c**, The stabilized efficiency of champion WBG perovskite module. **d**, Evolution of efficiency of an encapsulated WBG perovskite module. **e**,  $I$ - $V$  curves of the WBG perovskite module measured after light soaking for different durations.